Available online at www.sciencedirect.com
ScienceDirect
Journal of the European Ceramic Society 28 (2008) 617–631
www.elsevier.com/locate/jeurceramsoc

Joining of partially sintered alumina to alumina, titanium, Hastealloy and C–SiC composite using Ag–Cu brazes

R. Asthana[a,*], M. Singh[b]

[a] Department of Engineering & Technology, University of Wisconsin-Stout, Menomonie, WI 54751, USA
[b] Ohio Aerospace Institute, NASA Glenn Research Center, Cleveland, OH 44135, USA

Received 8 November 2006; received in revised form 16 June 2007; accepted 30 June 2007
Available online 20 September 2007

Abstract

The joining behavior of polycrystalline alumina sintered at different temperatures (1473–1773 K) and times (0.5–4 h) to itself and to Ti, Hastealloy and a CVI C–SiC composite using two Ag–Cu active metal brazes (Cusil–ABA and Ticusil) containing Ti has been evaluated. Partial densification and the resulting high porosity content of Al_2O_3 substrates sintered at low temperatures led to braze infiltration of Al_2O_3 pores in 20 min contact but no penetration occurred in dense Al_2O_3 substrates sintered at high temperatures. The scanning electron microscopy (SEM) and energy dispersive spectroscopy (EDS) examination of the joints showed that chemical reactions between Al_2O_3 and braze constituents formed a Ti-rich reaction layer at braze/Al_2O_3 interface regardless of the sintering conditions and degree of densification of the Al_2O_3. Some redistribution of the substrate and braze constituents across the joint interfaces was observed due to dissolution and interdiffusion. The Knoop microhardness of sintered alumina was consistent with the degree of Al_2O_3 densification achieved, and microhardness profiles across the joint regions displayed a minimum (~70–160 KHN) in the braze region and a maximum (1900–2012 KHN) in the alumina region. The polished CVI C–SiC composites led to better quality Al_2O_3/C–SiC composite joints and greater segregation of Ti at the composite/braze interface than unpolished composite specimens.

Keywords: Joining; Sintering; Porosity; Electron microscopy; Hardness; Infiltration; Al_2O_3; Ag–Cu brazes

1. Introduction

Alumina ceramics are joined to other ceramics and metals using a wide variety of liquid- and solid-phase bonding methods. Metals such as Ag, Al, Au, Cu, Fe, Nb, Mo, Ni, Pd, Ti and W and alloys such as steels, nichrome, Fe–Ni–Co and superalloys have been joined to alumina for various applications. Generally, material compatibility improves and joining becomes feasible when either the metal substrate is oxidized (oxide/alumina bond), alumina surface is metallized (metal/metal bond), or a wettability-enhancing chemical reaction (e.g., oxide dissolution, oxide reduction, etc.) is induced in the joint region, as in active metal brazing of ceramics. Brazing is a particularly simple and cost-effective ceramic joining technique. Generally, braze alloys contain Ti or another reactive metal (e.g., Zr, Nb, Cr or Y) to promote wetting, braze spreading and interfacial bonding. Besides alloying the filler metal with Ti, the ceramic may either be pre-coated with a Ti-bearing compound (e.g., TiH_2) that forms a layer of the active metal Ti on the oxide surface or molten alkali halide salts (e.g., alkaline earth halides of Ti) may be used while depositing Ti in order to prevent oxidation. Very high bond strengths are achieved with the use of active metal brazes in alumina joints.

Generally, high-density polycrystalline alumina ceramics are used in industrial brazing applications. This is because of the porosity in partially fired Al_2O_3 decreases the fracture strength of Al_2O_3 and is expected to inhibit braze wetting and spreading. Understanding braze spreading and penetration in porous ceramics has, however, considerable fundamental value and has been a focus of some studies.[1–4] For example, melt penetration of porous titanium carbonitride by Al–Mg–Si alloys,[1] porous AlN by Ag–Cu–Ti alloys,[2] porous zirconia by Mn,[3] and porous graphite by Cu–Ti and Cu–Cr[4] alloys has been studied. Scant information was, however, found on the effect of porosity in Al_2O_3 on its brazing response. In Mo–Mn film-coated Al_2O_3 in

---

* Corresponding author. Current address: ASRC Aerospace, MS 106-5, Ceramics Branch, NASA Glenn Research Center, Cleveland, OH 44135, USA.
E-mail address: asthanar@uwstout.edu (R. Asthana).

0955-2219/$ – see front matter © 2007 Elsevier Ltd. All rights reserved.
doi:10.1016/j.jeurceramsoc.2007.06.017

contact with an Ag–Cu brazing alloy, Nono et al.[5] observed that the alumina superficial pores were filled with Mo and Cu from the braze filled the pores in the Mo–Mn film. Generally, braze spreading is adversely affected by roughness and surface defects such as voids due to grain pull-out during polishing, which lead to large contact angles and poor wettability of porous ceramics by molten braze alloys.

The main objective of this study was to investigate the effect of porosity content in sintered polycrystalline Al_2O_3 on its joining response when the Al_2O_3 was brazed to itself using two Ag–Cu braze alloys containing different percentages of Ti. A related objective of the study was to join partially sintered alumina samples to pure Ti, a Ni-base superalloy (Hastealloy X), and a CVI C–SiC composite, the latter in both polished and unpolished conditions. All experiments simulated the worst case scenario of braze spreading on alumina: brazed joints were created using unpolished (as-sintered) Al_2O_3 substrates. The joints were characterized using optical and scanning electron microscopy (SEM) coupled with energy dispersive spectroscopy (EDS) and by microhardness measurements.

2. Experimental procedure

2.1. Sintering of alumina samples for the brazing study

High-purity Al_2O_3 powders (doped with 0.05% MgO) from Reynolds Metals Company, Bauxite, AR, USA, were used to fabricate the alumina substrates for the joining study. The average particle size based on the sedimentation analysis was ∼380 nm and the specific surface area (from the BET method) was $8.19\,m^2\,g^{-1}$. The sedimentation test results indicate that ∼60% powders are finer than ∼400 nm. Small disc shaped samples of Al_2O_3 with circular cross-section (25.4 mm diameter × 10 mm thickness) were pressed in a hydraulic press using cylindrical dies and punches at a constant load of 90 kN to obtain a consistent starting material for sintering. The compaction load of 90 kN (corresponding to a pressure of 175 MPa) was selected on the basis of experimentally observed saturation of green density at ∼90 kN load when the green samples were compacted at loads varying in the range of 45–155 kN (these loads correspond to a compaction pressure range of 89–306 MPa). Zinc stearate was used as the die lubricant to increase the pressure transmission ratio and facilitate green part ejection at the conclusion of compaction. Sintering of green Al_2O_3 coupons was done in a programmable tube furnace (CM Rapid Temp) under normal ambient air in the temperature range of 1473–1873 K for different time periods (0.5, 1, 2 and 4 h). The heating rate was set at $120°\,h^{-1}$.

2.2. Brazing

The Al_2O_3 samples sintered at different temperatures and for different times were sectioned across their diameters on a diamond saw to obtain test coupons for joining. The cutting and fixturing required considerable care as the brittle Al_2O_3 samples showed some tendency to crack. After sectioning, the as-fired specimens were cleaned in acetone for 15 min in an ultrasonic bath and used for brazing as such without polishing, surface preparation, or pre-annealing. The C–SiC composites used for joining were obtained from GE Power Systems Composites, Newark, DE, USA. These composites are reinforced with T-300 carbon fibers in a CVI SiC matrix. The composite panels were sliced into 25.4 mm × 12.5 mm × 2.5 mm pieces and dry polished using #320, #400 and #600 sand papers. Commercially pure Ti plates (Ti metal 75A) from Titanium Metals Corporation Inc., MO, USA and a Ni-base superalloy (Hastealloy X and nominal composition in wt.%: 22Cr–18.5Fe–9Mo–6W–1.5Co–0.5Mn–0.5Si–0.1C) were also cut into slices of the same size as the composite panels. Two Ag–Cu braze alloys (Cusil–ABA and Ticusil) from Morgan Advanced Ceramics, and containing different percentages of the active metal titanium were used in foil form (0.10–0.12 mm thick) for joining. The braze alloy compositions (in wt.%) are Cusil–ABA (63Ag–35.3Cu–1.75Ti) and Ticusil (68.8Ag–26.7Cu–4.5Ti). The braze liquidus temperatures of 1088 K for Cusil–ABA and 1173 K for Ticusil are below the lowest sintering temperature (1473 K) used in the study. Selected physical and mechanical properties of the braze alloys are given in Table 1.

Table 1
Selected braze property data

Braze	*E* (GPa)	YS (MPa)	TS (MPa)	CTE (/C)	El (%)	*K* (W/mK)
Cusil–ABA	83	271	346	18.5×10^{-6}	42	180
Ticusil	85	292	339	18.5×10^{-6}	28	219

E: Young's modulus; YS: yield strength; TS: tensile strength; CTE: coefficient of thermal expansion; El (%): percent elongation; *K*: thermal conductivity.

The joining procedure consisted of placing two braze foils between the plaques of the substrate materials, and heating the assembly under vacuum (∼10^{-6} Torr) to the brazing temperature (typically 15–20° above the braze liquidus) under 0.4 N normal load. After 20 min isothermal soak at the brazing temperature, the joints were furnace cooled at a controlled rate.

2.3. Joint characterization

For metallographic examination, the brazed samples were mounted in epoxy and polished to optical finish. The microstructure of the joints was examined by optical microscopy and scanning electron microscopy (SEM) (model JEOL-840) coupled with energy dispersive spectroscopy (EDS). Microhardness measurements were made across the joint interfaces using a Knoop microindenter on a Buehler's MicroMet-2001 machine under a load of 200 g and a loading time of 10 s.

3. Results and discussion

3.1. Sintering of alumina substrates

Fig. 1(a) shows the average bulk density of MgO-doped Al_2O_3 samples as a function of sintering temperature for four

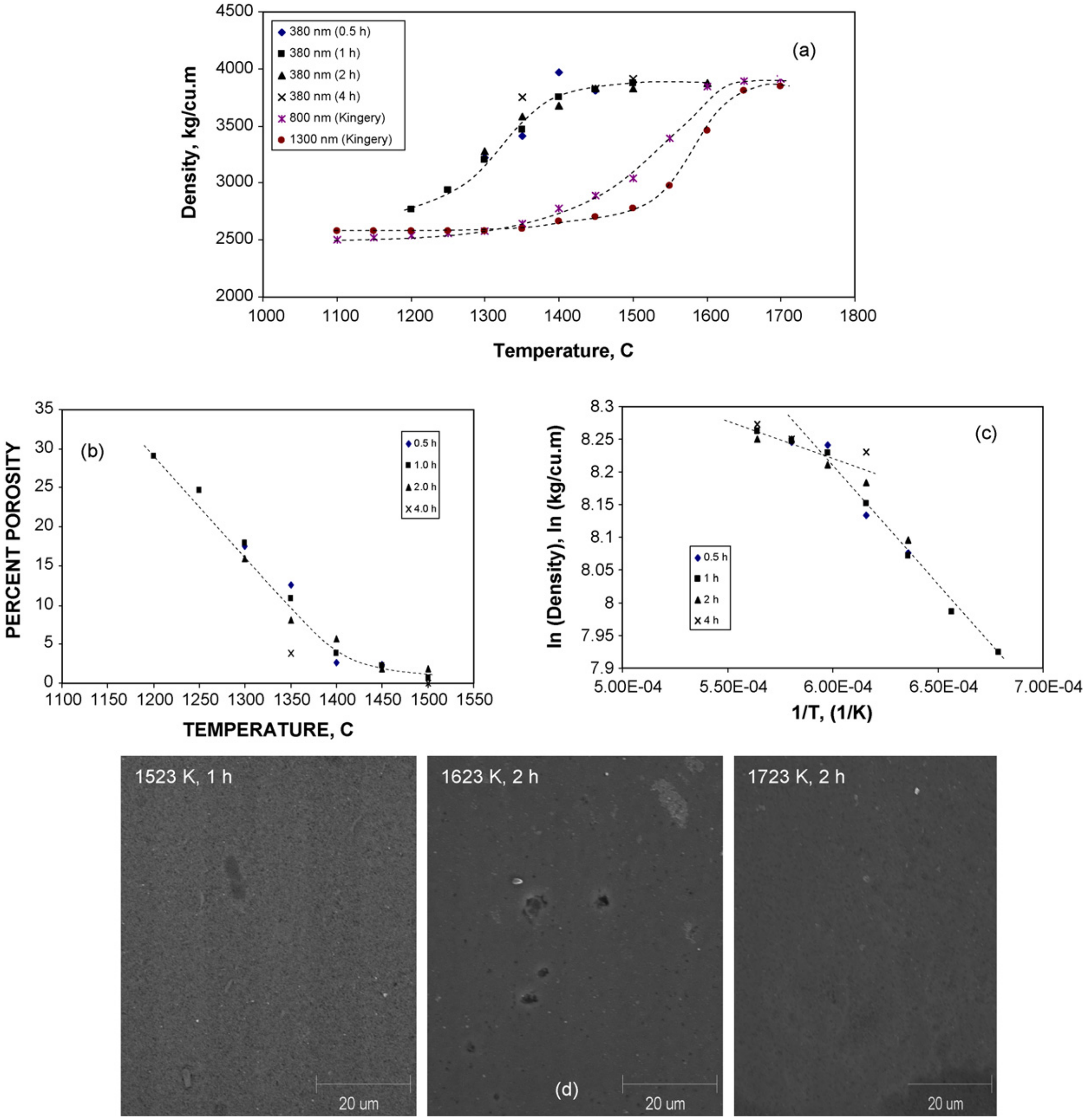

Fig. 1. (a) Average density and (b) percent porosity in MgO-doped sintered Al_2O_3 (nominal size: 380 nm) as a function of sintering temperature for different sintering times (literature data from Ref. [6] on coarser alumina are shown in (a) for comparison), (c) shows an Arrhenius plot of natural logarithm of density vs. inverse of absolute sintering temperature. Trend-lines are shown to guide the eye. The density data are based on measurements made on 370 separate samples. (d) SEM views of Al_2O_3 substrates sintered at different temperatures and times.

different sintering times. The density data are based on measurements made on 370 individual Al_2O_3 test coupons that were fired in air for different temperatures and times. The bulk density was calculated from weight and volume measurements on each sample from which total porosity content was estimated. The percent bulk porosity was estimated from: porosity $(\%) = ((d_{\text{theor}} - d_{\text{exp}})/\text{d}_{\text{theor}}) \times 100$, where d_{theor} is the theoretical density of fully densified alumina ($d_{\text{theor}} = 3970\,\text{kg}\,\text{m}^{-3}$) and d_{exp} is the measured bulk density. Fig. 1(a) also compares the literature data[6] on densification of coarser (1300 and 800 nm) Al_2O_3 powders with the densification behavior of compacts made from the fine (380 nm) powders that were used in the present study. It can be noted that compacts of fine powders exhibit faster densification kinetics; this suggests the importance of using fine ceramic powders for rapid or low-temperature sintering of ceramics. Fig. 1(b) shows a plot of percent porosity as a function of sintering temperature. Trend-lines are shown to guide the eye. As expected, the porosity curve exhibits a trend opposite to that of density. Densification is accompanied by a decrease in the total porosity content with increasing temperature. Near-zero porosity (full-densification) was attained for 380 nm size powders at ∼1773 K. In addition, initial densification was faster at high sintering temperatures.

Fig. 1(c) shows an Arrhenius plot of the density data as natural log of the bulk density versus inverse absolute temperature. Again, a trend-line to guide the eye is shown in the figure. Two linear regimes, each reminiscent of an Arrhenius-type relationship (i.e., $d = d_0 \exp[-Q/RT]$, with d and d_0 being the density at a temperature T and at room temperature, respectively) can be identified in Fig. 1(c). This could possibly indicate a change in the activation energy and the sintering mechanism with increasing temperature (no further investigation of this transition was pursued). Fig. 1(d) shows the SEM views of the Al_2O_3 substrates sintered at different temperatures and times. Finely dispersed porosity is noticed in the low-temperature sample (1523 K and 1 h) whereas greater densification and near-zero porosity is achieved in the samples sintered at high temperature (1723 K and 2 h).

3.2. *Joint microstructures and composition*

3.2.1. *Al_2O_3/Cusil–ABA/Al_2O_3 joints*

Fig. 2 shows the SEM views of joint microstructures in Al_2O_3/Cusil–ABA/Al_2O_3 joints made using Al_2O_3 samples sintered at 1773 K for 1 h (Fig. 1(a and b)), 1723 K for 2 h (Fig. 2(c)), 1623 K for 2 h (Fig. 2(d)), 1523 K for 1 h (Fig. 2(e)) and 1473 K for 1 h (Fig. 2(f and g)), respectively. The braze matrix displays the characteristic two-phase eutectic microstructure of the Ag–Cu alloy, and the joint interfaces in all the samples of Fig. 2 show the interface reaction layers approximately 2–5 μm in thickness. The reaction layer thickness appears to depend upon the substrate sintering temperature, with thicker reaction layers forming in the low-temperature samples (Fig. 2(d and g)) than in the high-temperature samples (Fig. 2(b and c)). Quantitative measurements of reaction layer thickness as a function of temperature were not attempted; the difference in the reaction layer thickness is presumably related to the differences in the size and percentage of porosity in sintered samples (with low-temperature samples exhibiting greater porosity and larger effective area of contact for solid/liquid reaction than high-temperature samples).

The Al_2O_3/Cusil–ABA interfaces in the low-temperature samples (Fig. 2(e, f and g)) exhibit braze penetration in the bottom half of the sintered Al_2O_3 coupons in the direction of the gravity vector. Greater infiltration is evident in the sample sintered at 1473 K for 1 h (Fig. 2(f and g)) than in the sample sintered at 1523 K for 1 h (Fig. 2(e)). No such infiltration is, however, evident in samples sintered at higher temperatures (Fig. 2(a–d)). With a substantial amount of interconnected porosity in the low-temperature Al_2O_3 samples, the filler metal is drawn (wicked) into the porous substrate, leaving metal-starved regions (voids) near the top interface as seen in Fig. 2(e and f). The void at the top Al_2O_3/braze interface in these figures presumably develops due to the finite reservoir effect (fixed braze volume) rather than

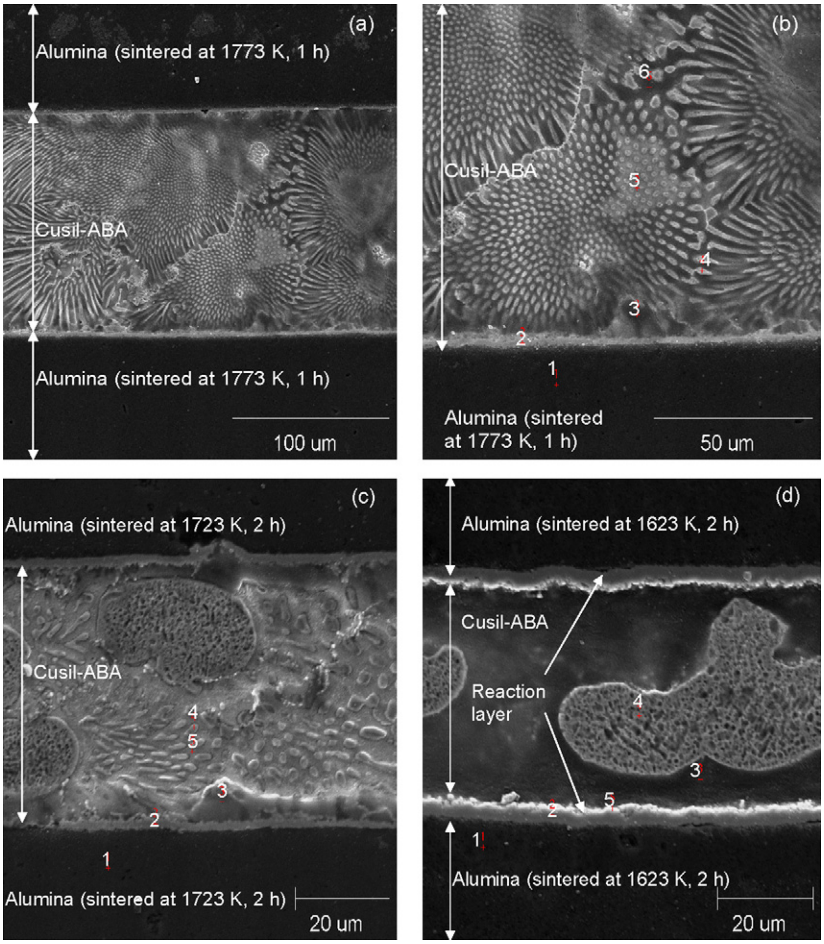

Fig. 2. Al_2O_3/Cusil/Al_2O_3 joints made under the conditions marked in the figures.
]

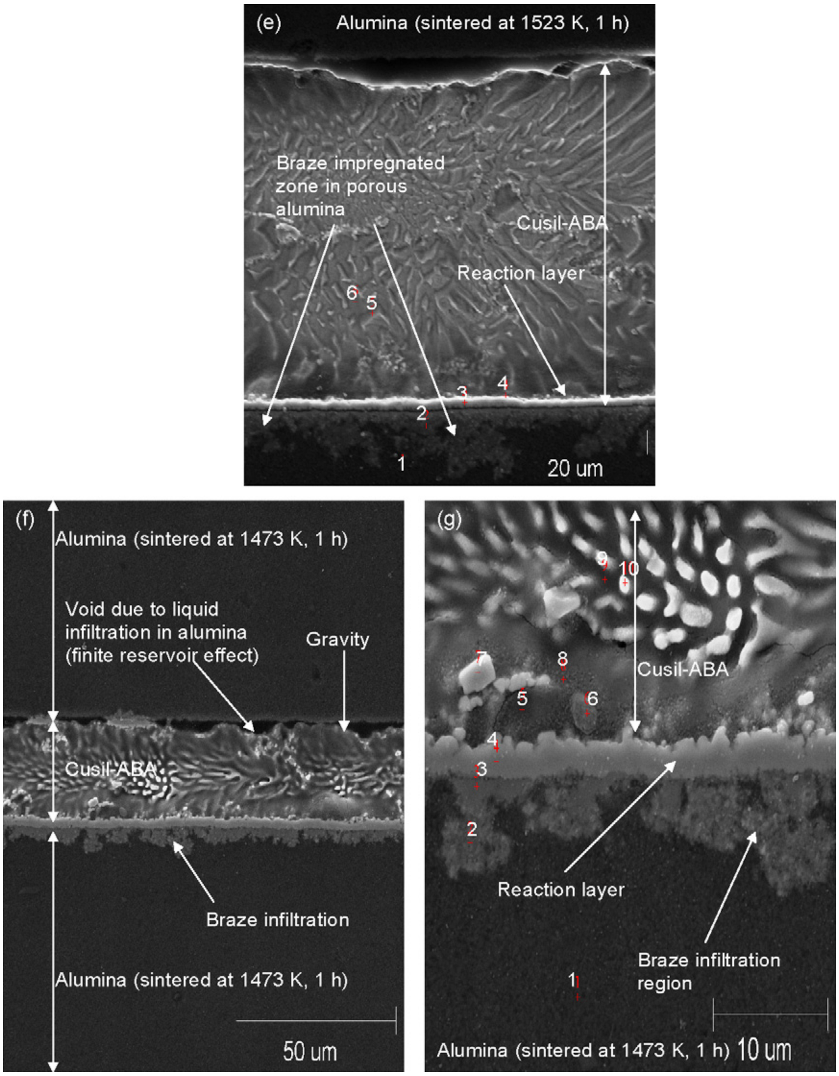

Fig. 2. (*Continued*).

due to the solidification shrinkage. This is borne out by the fact that the joints made from Al_2O_3 samples sintered at high temperatures (Fig. 2(a–c)) do not show such voids. Braze penetration in the porous Al_2O_3 samples can occur only if a critical wetting condition is satisfied, i.e., the contact angle, $\theta < 90^\circ$. This is because for pore penetration to occur spontaneously by molten braze, the capillary pressure, P_c (i.e., the pressure differential across the liquid front at pore entrance) should be negative[7,8], where $P_c = -2\sigma_{lv} \cos\theta/r$ and σ_{lv} is the surface tension of the braze and r is the effective pore radius. Thus, for $\theta < 90^\circ$, $P_c < 0$ and wicking of molten braze will occur. For $\theta > 90^\circ$, $P_c > 0$ and an external pressure will be needed to drive the liquid in the pore. The braze infiltration of the porous Al_2O_3 substrates is discussed in some depth in the next section.

Fig. 3 shows the EDS results on elemental distribution across the Al_2O_3/Cusil–ABA interface at the locations marked on SEM photomicrographs in Fig. 2(b–e and g). The EDS data qualitatively represent the relative atomic percentage of alloying elements at different locations in the structure. The EDS point locations in Fig. 3 (and in Figs. 5, 7 and 9) do not represent distance or a microstructure length scale but are intended to be merely representative of certain locations in the joint. The curves connecting the individual data points should not be construed as implying a trend; they are used merely as visual aids.

The evidence of braze penetration into porous Al_2O_3 (1473 K and 1 h) is noted from the presence of Ag, Cu and Ti at point '2' (Fig. 2(g)) which is within the alumina region for this particular sample (the Ag, Cu and Ti profiles are shown in Fig. 3(a, c and e), respectively). The points marked '2' in Fig. 2 for all samples (except the sample of Fig. 2(e and g)) lie within the reaction product layer at the Al_2O_3/Cusil–ABA interface. The EDS composition profiles (Fig. 3) at this point show the presence of Cu, Ti and some Al in the reaction layer; this is also true for point '4' in the 1473 K and 1 h sample, which lies within the reaction layer (Fig. 2(g)). The reaction layers in all the samples have particularly high concentration of Ti (Fig. 3(c)), which suggests the possible formation of titanium oxides at the braze/alumina interface. These titanium oxides can form from the reduction of alumina by Ti according to the reactions given below:

$$Al_2O_3 + (3/2)Ti \rightarrow 2Al + (3/2)TiO_2$$

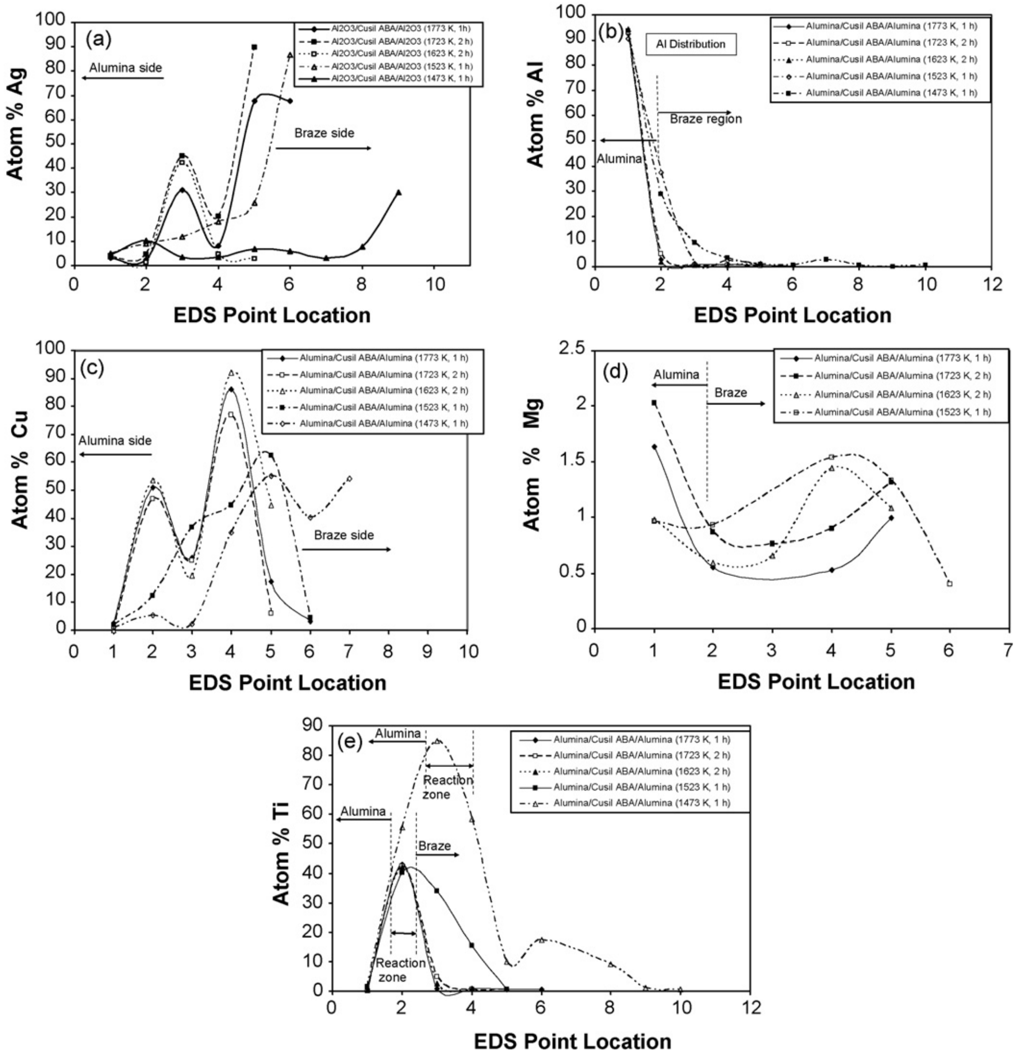

Fig. 3. Relative atomic percentages of major alloying elements across the joint interfaces in alumina/Cusil ABA/alumina joints: (a) Ag, (b) Al, (c) Cu, (d) Mg and (e) Ti. The EDS locations are shown in Fig. 2. The boundaries marked between different regions of the joints are approximate. The EDS point locations are intended to be representative of certain locations. The curves connecting the data points are not meant to imply a trend; they are used merely as visual aid to identify data for different joints on the same graph.

$$Al_2O_3 + 3Ti \rightarrow 2Al + 3TiO$$

$$Al_2O_3 + 2Ti \rightarrow 2Al + Ti_2O_3$$

$$Al_2O_3 + (9/5)Ti \rightarrow 2Al + (3/5)Ti_3O_5$$

$$Al_2O_3 + (12/7)Ti \rightarrow 2Al + (3/7)Ti_4O_7$$

Most of the oxides of titanium are very stable as shown by the large negative change in the Gibb's free energy, ΔG, for their formation at 1123 K (an arbitrarily selected temperature within the brazing temperature range used for Cusil–ABA and Ticusil). The values of ΔG, calculated using the software HSC Chemistry Version 4.1 (Outokumpu Ra, Oy, Finland) for the different oxides of Ti at 1123 K are: TiO_2 (−740.7 kJ), TiO (−434.9 kJ), Ti_4O_7 (−2704.8 kJ) and Ti_3O_5 (−1959.1 kJ).

The reaction product layer between Al_2O_3 and AgCuTi braze alloys has been experimentally identified in the literature[9,10] as comprising predominantly of the TiO phase near the Al_2O_3 boundary, and the Ti_3Cu_3O phase near the braze side of the Al_2O_3/AgCuTi interface. Similarly, in Al_2O_3/Ag–38Cu–3.7Ti at 1223 K, the interface consists of a layer of TiO_x ($x = 0.55$–0.6) situated on the ceramic side, and a layer of the metal-like compound $Ti_3(CuAl)_3O$ formed in contact with the braze alloy.[11] In addition, Cu_2Ti_4O and $CuAlO_2$ phases may form but their formation is thermodynamically less probable than the above-mentioned phases.

3.2.2. *Infiltration of the porous Al_2O_3 substrate by Cusil–ABA*

It was pointed out in the previous section that Al_2O_3/Cusil–ABA interfaces in the low-temperature samples (Fig. 2(e, f and g)) exhibited braze penetration in the bottom half of the sintered Al_2O_3 coupons. Furthermore, greater infiltration is evident in the sample sintered at 1473 K for 1 h (Fig. 2(f and g)) than in the sample sintered at 1523 K for 1 h (Fig. 2(e)). In this section, the process of pore penetration in the Al_2O_3 substrates is analyzed in some depth.

Literature data[11–13] on contact angle of Ag–Cu–Ti brazes in contact with alumina ceramics show that Ti significantly lowers the contact angle of Ag–Cu alloys on Al_2O_3. The drop in the contact angle is rapid in the presence of Ti in the alloy, and the condition $\theta < 90^\circ$ is rapidly attained. The extent of penetration of reactive filler in porous ceramics depends also upon the nature of the reaction products, volumetric changes accompanying formation of reaction products, the porosity and the morphology (e.g., discontinuity) of the reaction layer. For example, Cu–Ti and Cu–Cr alloys wet the porous graphite but Cu–Cr alloys form a reaction layer that is very dense and effectively seals the open porosity in the carbon, thus blocking melt penetration. With Ti in place of Cr as an alloying element in Cu, the reaction-formed TiC layer is discontinuous and non-homogenous, which allows pore penetration by the molten braze and continued infiltration.[4] Even in the case of a dense and impervious reaction layer, the relative rates of melt penetration and the rate of formation of the reaction layer will play an important role; if the reaction rate is slow, then significant melt penetration could occur before the reaction products choke the liquid flow.[14]

Modeling of reactive infiltration either invokes a modified Darcy's law to account for a time-dependent permeability[15] or uses a shrinking core model[16–18] which assumes that the reaction front moves into the porous solid, leaving behind solid reaction products and fluid. These models assume a constant contact angle during flow, which is incompatible with the situation in most reactive systems where wetting is dynamic and the contact angle changes with time[7,19] with the result that capillary forces are modulated during the flow. Analytical models of infiltration to take into account both solid/liquid reaction and dynamic wetting have been presented in Refs.[20,21], and the phenomenon of reactive infiltration in high-temperature systems have been discussed in Refs.[8,22,23]

In the present context, the porous Al_2O_3 substrate can be modeled as a solid with an array of parallel, right cylindrical pores of some averaged or effective radius, R. Neglecting the pore interconnectedness will introduce some numerical error in the process kinetics but the important effects of surface porosity on spreading and penetration behaviors can still be identified. For capillary rise under quasi-steady state and at short times, the kinetics are given from the Washburn equation:

$$h\frac{dh}{dt} = \frac{\rho R^2}{8\mu}\left(\frac{2\sigma_{lv}\cos\theta}{\rho R} - gh\right) \tag{1}$$

where ρ is the density of melt, g the acceleration due to gravity, R the capillary radius, μ the viscosity, σ_{lv} the surface tension and h is the penetration distance. If $h \ll H$, where H is the height to attain hydrostatic equilibrium ($H = 2\sigma_{lv}\cos\theta/\rho gR$), then the gravity term in Eq. (2) can be ignored. Under these conditions, a parabolic solution of the form $h^2 = kt$ (where $k = R\sigma_{lv}\cos\theta/2\mu$) is obtained which is consistent with the experimental penetration kinetics in a number of low- and high-temperature systems. There are several other special cases of practical interest that emerge from a detailed analysis of the equation of motion of a liquid in a capillary.[24]

The contact angle, θ, in a number of ceramic/metal systems is known to decrease exponentially with time[12–14] according to the equation: $\theta(t) = \theta_\infty + \theta_\infty e^{(B-At)}$ where θ_∞ is the equilibrium contact angle and A and B are system-specific constants, usually derived from the experimental θ–t data. For reactive infiltration with a shrinking pore, the temporally decreasing contact angle, $\theta(t)$ and pore radius, $R(t)$, will both increase the capillary pressure, P_c, at the meniscus [where $P_c = \sigma_{lv}\cos\theta(t)/R(t)$]. For the diffusion-controlled capillary penetration with a time-dependent θ, the capillary radius decreases parabolically with time (ignoring the geometrical complexities due to curvature of the reaction front):

$$R(t) = R_0 - m\sqrt{t} \tag{2}$$

where m is a parabolic reaction rate constant and R_0 is the initial capillary radius at $t = 0$ (here the product phase has a higher specific volume than the parent solid so $R(t)$ decreases with time). In the presence of Ti in Ag–Cu braze alloys in contact with Al_2O_3 substrates the contact angle is known to rapidly stabilize to its equilibrium value θ_∞, and for the experimental brazing time of 20 min that was used in the experiments, the dynamic wetting effects may be ignored, and a constant value of θ ($=\theta_\infty$) may be used. For the special case of diffusion-controlled reactive infiltration with negligible liquid weight and constant θ ($=\theta_\infty$), substitution of Eq. (2) in Eq. (1) and integration of the resulting expression yields the following relationship between infiltration depth, h and infiltration time, t[14]:

$$\frac{2\mu h^2}{\sigma_{lv}} = \cos\theta_\infty\left[R_0 t - \frac{2m}{3}t^{1.5}\right] \tag{3}$$

Eq. (3) was used to estimate the effective pore radius in the Al_2O_3 substrates sintered at 1473 K for 1 h (Fig. 2(g)). The braze infiltration distance in the Al_2O_3 in Fig. 2(g) is ∼10 μm for a brazing time of 20 min. The values of the surface tension, σ_{lv}, of liquid Cusil–ABA (63Ag–35.3Cu–1.75Ti) and Ticusil (68.8Ag–26.7Cu–4.5Ti) are taken to be $\sigma_{lv} \sim 0.987\ \mathrm{J\,m^{-2}}$ (average value for Ag–28Cu[25]) and the viscosity, μ, is taken to be 4.349 mPa s (value for Ag–40Cu[26]). The equilibrium contact angle, θ_∞, of AgCuTi (3–8% Ti) alloy on alumina is ∼12°.[9–11]

Two conditions need to be specified in order to apply Eq. (3) to the infiltration of porous Al_2O_3 substrates: (1) justification for the application of the diffusion-control mechanism for the reaction of Al_2O_3 with the AgCuTi alloy; and (2) the magnitude of the parabolic diffusion rate constant, m, for the reaction of Al_2O_3 with the braze. Voytovich et al.[11] studied the kinetics at 900 °C of the reaction between Al_2O_3 and a Ag–48.1Cu–3.1Ti (at.%) alloy. Their experimental data clearly show that the reaction layer thickness increased linearly with $\sqrt{t}$ suggesting a diffusion-control mechanism. Further, the parabolic rate constant, m, extracted from their reaction kinetics data yielded a value of $m = 0.129$ μm/s. Using this value of m, and the above referenced values of σ_{lv}, θ_∞ and μ, together with $t = 1200$ s and $h \sim 10$ μm, Eq. (3) yielded a realistic initial pore diameter ($2R_0$) of ∼6 μm in the Al_2O_3 substrate. In contrast, the classical solution, $h^2 = kt$, where $k = R\sigma_{\mathrm{lv}} \cos\theta/2\mu$, with negligible weight of the liquid and with a constant pore diameter (i.e., neglecting the reaction-induced pore shrinkage) yields an unrealistic pore diameter of atomic size for the same depth of penetration $h \sim 10\,\mu\mathrm{m}$. Conversely, a constant pore diameter of 6 μm in the classical solution yields a penetration distance of 1095 μm, which is two orders of magnitude larger than the penetration distance observed in Fig. 2(g). Whereas these calculations are undeniably somewhat crude they nevertheless indicate that experimental observations on reactive infiltration of porous alumina by molten braze are amenable to interpretation with the help of models of reactive infiltration phenomenon. Infiltration in the present case will be limited by the finite reservoir effects which the above calculations do not consider. This is because a finite braze volume will restrict the extent of infiltration in the porous alumina. The effective drawing area of braze equals the contact area between braze and the Al_2O_3 substrate. If the number density of pores (i.e., number of pores per unit area) in the porous Al_2O_3 substrate were known, then the volumetric depletion of the braze can be estimated from the kinetics of the reactive infiltration discussed above.

Finally, the assumption to neglect the weight of the liquid braze permeating the porous Al_2O_3 substrates is acceptable because the capillary length ($L_c = [\sigma_{\mathrm{lv}}/\rho g]^{0.5}$) is appreciably larger than the effective pore diameter. This is true for the present case because for Ag–45Cu, $L_c \approx 0.0032$ m or 3200 μm (with the density and surface tension of AgCuTi as $\rho = 9790\,\mathrm{kg\,m^{-3}}$ and $\sigma_{\mathrm{lv}} \sim 0.987\,\mathrm{J\,m^{-2}}$).

3.2.3. Al_2O_3/Ticusil/Al_2O_3 joints

Fig. 4 shows the SEM photomicrographs of the Al_2O_3/Ticusil/Al_2O_3 joints made using sintered Al_2O_3 substrates containing varying degree of porosity. There is no evidence of braze penetration in high-density Al_2O_3 joints (Fig. 4(a–d)) whereas the low-density Al_2O_3 joints (Fig. 4(f)) shows some braze penetration. In all cases, a reaction layer has formed at the Al_2O_3/Ticusil interface and the joints appear to be microstructurally sound. The EDS examination (Fig. 5) shows the Ti enrichment in the reaction zone at the interface (Fig. 5(e)), with the highest interfacial Ti concentrations occurring in the least dense Al_2O_3 substrates (1523 K and 2 h) and the smallest Ti concentrations in the reaction zone of the most dense substrates (1723 K and 4 h). Besides Ti enrichment, the reaction layer also has high Cu concentrations (Fig. 5(c)), which suggests that TiO and Ti_3Cu_3O phases may have formed in this region as alluded to above. In addition, some dissolution of MgO from the Al_2O_3 substrates and diffusion of the surface active element, Mg, into the reaction zone and the braze region are noted (Fig. 5(d)).

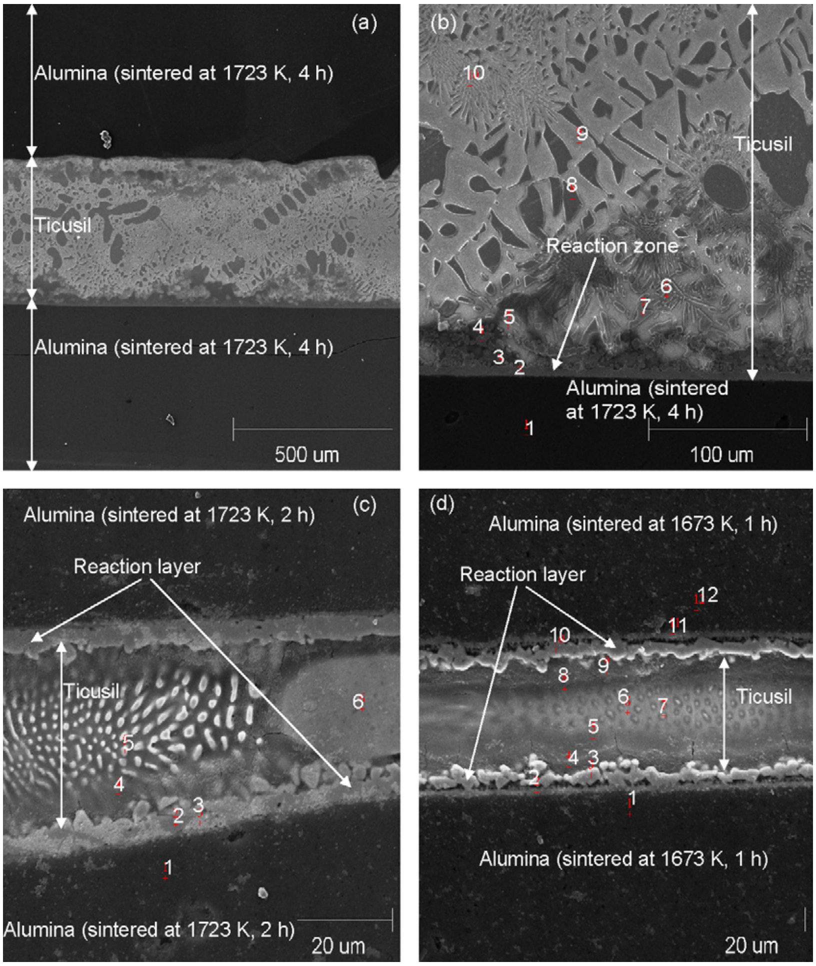

Fig. 4. Al_2O_3/Ticusil/Al_2O_3 joints made under the conditions marked on the figures.

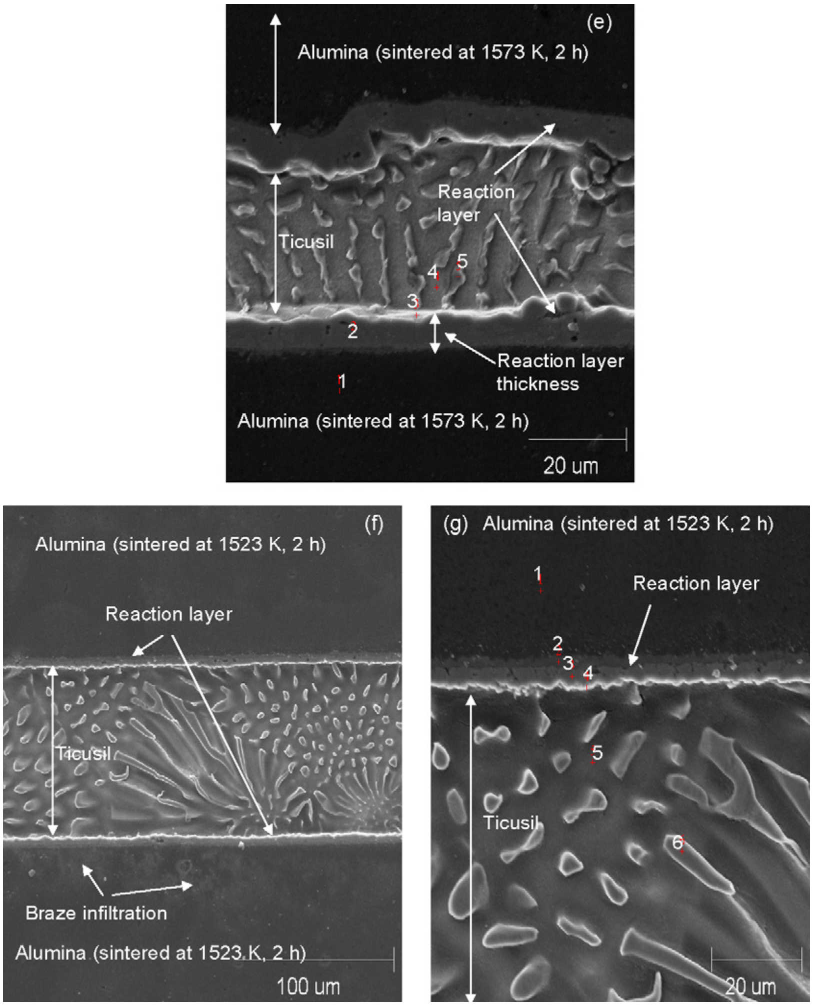

Fig. 4. (*Continued*).

The braze alloy Ticusil contains more Ti (4.5%) than Cusil–ABA (1.75%). As stated in the preceding section, Ti in the Ag–Cu braze improves the wettability of alumina and lowers the contact angle, θ; higher Ti contents yield better Al_2O_3/braze wetting. For example, in the Al_2O_3/Cu–Ti system, an increase in Ti content progressively decreases the equilibrium value of θ from around 152° at 0% Ti to 10–12° at 8% Ti[9–11], thereby making the system nearly fully wettable from initially non-wettable. In addition, the slightly higher Ag content of Ticusil than Cusil–ABA is likely to enhance the activity of Ti, leading to even better braze wetting and spreading of Ticusil than Cusil–ABA. The initial contact angle of ~150° at 1173 K of nearly eutectic Ag–Cu alloys containing 3% Ti drops to ~15° in about 20 min contact on sapphire in high vacuum.[9] This occurs because of chemical reaction-induced wettability which is promoted by the formation of TiO_x ($x = 0.55$–0.6) and $Ti_3(CuAl)_3O$ phases at the interface.

3.2.4. Al_2O_3/Cusil–ABA/C–SiC and Al_2O_3/Ticusil/C–SiC joints

Ceramic-matrix composites (CMC's) such as C–SiC are useful for demanding aerospace and critical ground-based applications in hypersonic aircraft thermal structures, advanced rocket propulsion thrust chambers, turbo pump blisks/shaft attachments, brake disks and numerous other advanced components. Most such applications require joining the CMC to metals, alloys, ceramics, or composites. Fabrication of complex large-scale structural components requires robust integration technologies capable of assembling smaller, geometrically simple CMC parts. Brazing is an ideal joining technique for such a purpose. In a series of recent publications,[27–34] the authors have reported on the brazing of advanced ceramics and CMC's (C–SiC, SiC–SiC and C–C), joint microstructure and properties.

Fig. 6 shows the SEM micrographs of Al_2O_3/Cusil–ABA/C–SiC and Al_2O_3/Ticusil/C–SiC composite joints. The effect of polishing the composite substrate on the joint microstructure is also shown in this figure for the Al_2O_3/Cusil–ABA/C–SiC joints. Use of polished CVI C–SiC composite substrates improves the joint integrity with Al_2O_3 (Fig. 6(c)) as compared to unpolished substrates (Fig. 6(d)) which show interfacial decohesion along the braze/composite interface.

Monolithic ceramics are generally polished prior to brazing to improve the flow characteristics of the braze alloy. Unlike monolithic ceramics, however, the effect of polishing of ceramic composite substrates on the quality of the brazed joints is less well established although a general response similar to that of

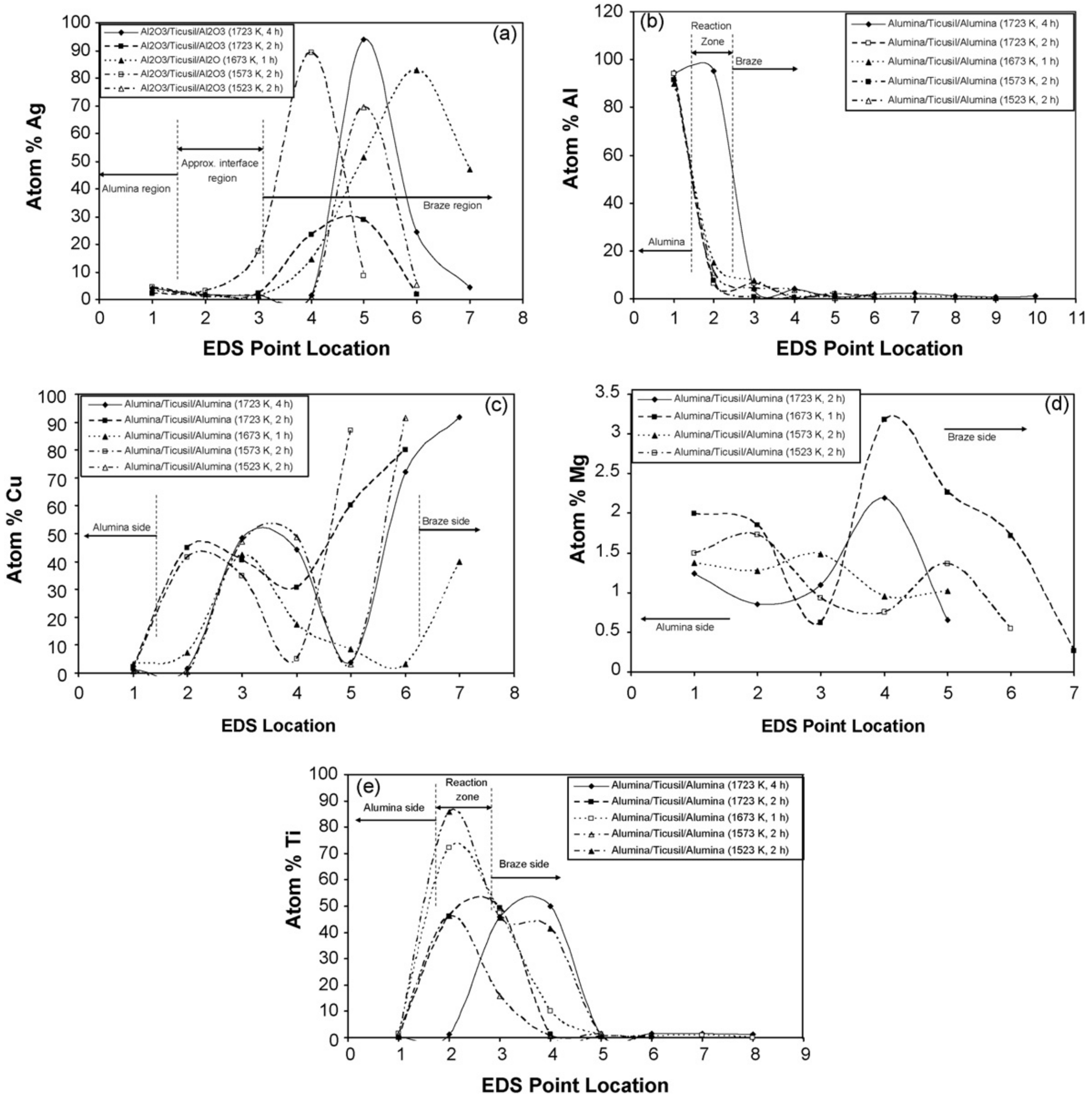

Fig. 5. Relative atomic percentages of major alloying elements across the joint interfaces in alumina/Ticusil/alumina joints: (a) Ag, (b) Al, (c) Cu, (d) Mg and (e) Ti. The EDS locations are shown in Fig. 4. The boundaries marked between different regions are only approximate. The curves connecting the data points are not meant to imply a trend.

monolithic ceramics is expected. For example, in Al_2O_3/SiC composites, polishing prior to brazing reduced the defect population and led to significantly higher joint strength.[35] However, polishing may also introduce new surface and sub-surface damage in the ceramic matrix such as grain and whisker or fiber pull-out as well as porosity. Even in monolithic ceramics such as Al_2O_3, polishing of as-fired alumina prior to brazing can introduce surface damage, which may require re-firing of polished alumina to heal the surface defects. Additional surface roughness and sub-surface damage may be introduced while vacuum heating the substrate during brazing. In fact, opening-up of partially closed pores during heating under vacuum has been observed.[36] For example, vacuum heating of graphite substrates that were pre-polished to different average initial roughness values led to an increase in the surface roughness by 41–227%.[36] Such a dramatic effect of pre-heating on surface roughness is not uncommon, and will alter the spreading and flow of molten braze in the joint region.

From the viewpoint of braze spreading, the contact angle, θ, may increase with increasing roughness if the system is non-wettable (i.e., $\theta > 90^\circ$), making braze spreading even more difficult due to roughness. But θ will decrease with increasing roughness if the system is wettable (i.e., $\theta < 90^\circ$). Even in reactive systems in which chemical reactions induce wetting, the initial braze spreading will be facilitated by a smooth, polished substrate because the wettability-enhancing reactions are usually preceded by an incubation stage during which the spreading is controlled by the interfacial tensions of the pristine phases. Thus, polishing of the substrate is generally beneficial as it is actually observed in Fig. 6(c and d) provided significant surface and sub-surface damage is not introduced during the polishing operation.

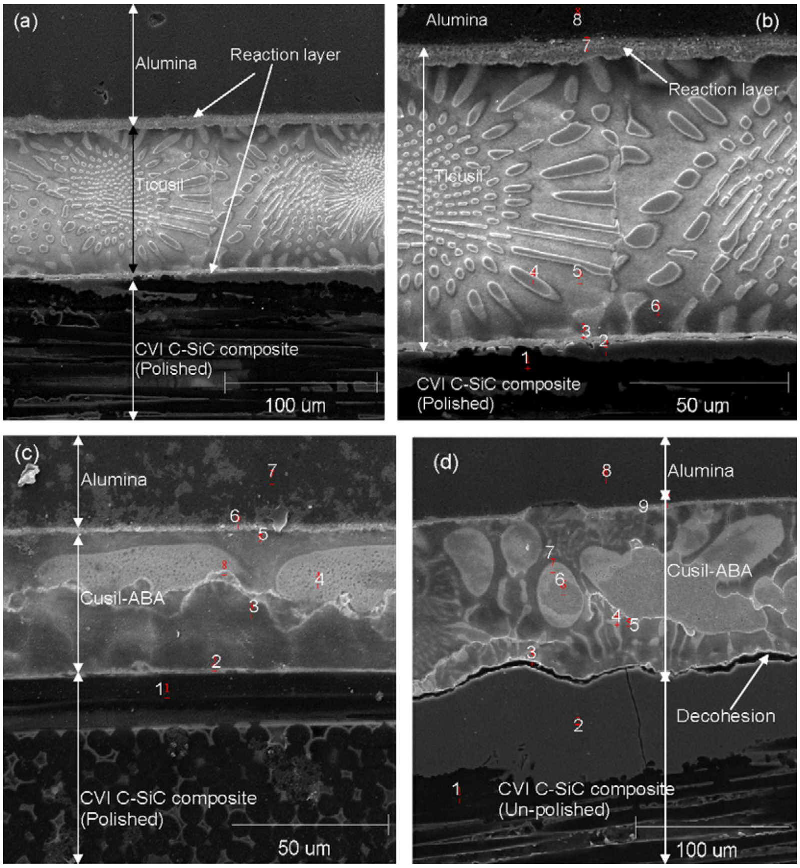

Fig. 6. CVI C–SiC composite/Al_2O_3 joints created using (a and b) Ticusil and (c and d) Cusil–ABA. The effect of polishing the composite substrate is displayed in (c) and (d) for Cusil–ABA joints. The Al_2O_3 substrates used were sintered at 1673 K for 2 h.

The EDS results on the distribution of elements in the joint regions of samples of Fig. 6 are shown in Fig. 7. The composite side of the braze/C–SiC composite interface (point '1' in Fig. 6(b–d)) shows the presence of Ag, Cu and Ti and small amounts of Al and Mg. As with the other joints examined in this study, there is considerable Ti enrichment of the interface region suggesting the formation of a Ti-rich interfacial compound as discussed in the preceding section.

The segregation of Ti at the composite/braze interface is due to the high chemical affinity of Ti toward C, which promotes wetting and bonding. At the brazing temperature, rapid diffusion and adsorption of Ti, as well as its chemical reaction with the carbon in the C–SiC composite substrate could form stoichiometric carbide (TiC) as well as sub-stoichiometric carbides (e.g., $TiC_{0.95}$, $TiC_{0.91}$, $TiC_{0.80}$, $TiC_{0.70}$, $TiC_{0.60}$ and $TiC_{0.48}$). In addition, formation of silicide phases at the interface from the reaction of Ti and Si (from the SiC) is a distinct possibility. These chemical reactions will promote the bonding provided the interfacial roughness of the unpolished substrate does not hamper braze spreading and physical contact.

3.2.5. Al_2O_3/Cusil–ABA/Ti and Al_2O_3/Cusil–ABA/Hastealloy X joints

The SEM views of the Al_2O_3/Cusil–ABA/Hastealloy and Al_2O_3/Cusil–ABA/Ti joints are shown in Fig. 8(a and b), respectively. Unlike the well-demarcated Al_2O_3/Cusil–ABA boundary in these figures, the Cusil–ABA/Hastealloy and Cusil–ABA/Ti boundaries are rather diffused because of extensive dissolution and interdiffusion of the metal substrate in the molten braze at these boundaries. This has led to a rather gradual transition in the metallurgical structure of the joints at the Cusil–ABA/Hastealloy and Cusil–ABA/Ti interfaces. Nickel and titanium have very strong chemical affinity for each other. In addition, Ni dissolves extensively in Cu–Ag alloy melts. These factors will favor a gradual transition in the interface structure. The EDS composition analysis (Fig. 9) shows the preferential concentration of Mg and Ti at the Al_2O_3/Cusil–ABA interface in both Ti and Hastealloy joints; in addition presence of Ag and Cu is noted in the interface region. There is no significant interfacial segregation of any of the major alloying elements (Cr, Mo, W and Co) in the Al_2O_3/Hastealloy X joints, although a Ni-rich phase forms in the vicinity of the interface. The joint interfaces are devoid of structural imperfections such as cracks or microvoids.

3.3. Microhardness

The Knoop microhardness profiles across the joint regions are shown in Fig. 10. In both Al_2O_3/Cusil–ABA/Al_2O_3 (Fig. 10(a)) and Al_2O_3/Ticusil/Al_2O_3 (Fig. 10(b)) joints, the minimum hardness (∼70–160 KHN) occurs in the braze region and the maximum hardness (∼1900–2012 KHN) in the Al_2O_3 regions. The microhardness profiles of Al_2O_3/Ti and Al_2O_3/CVI C–SiC

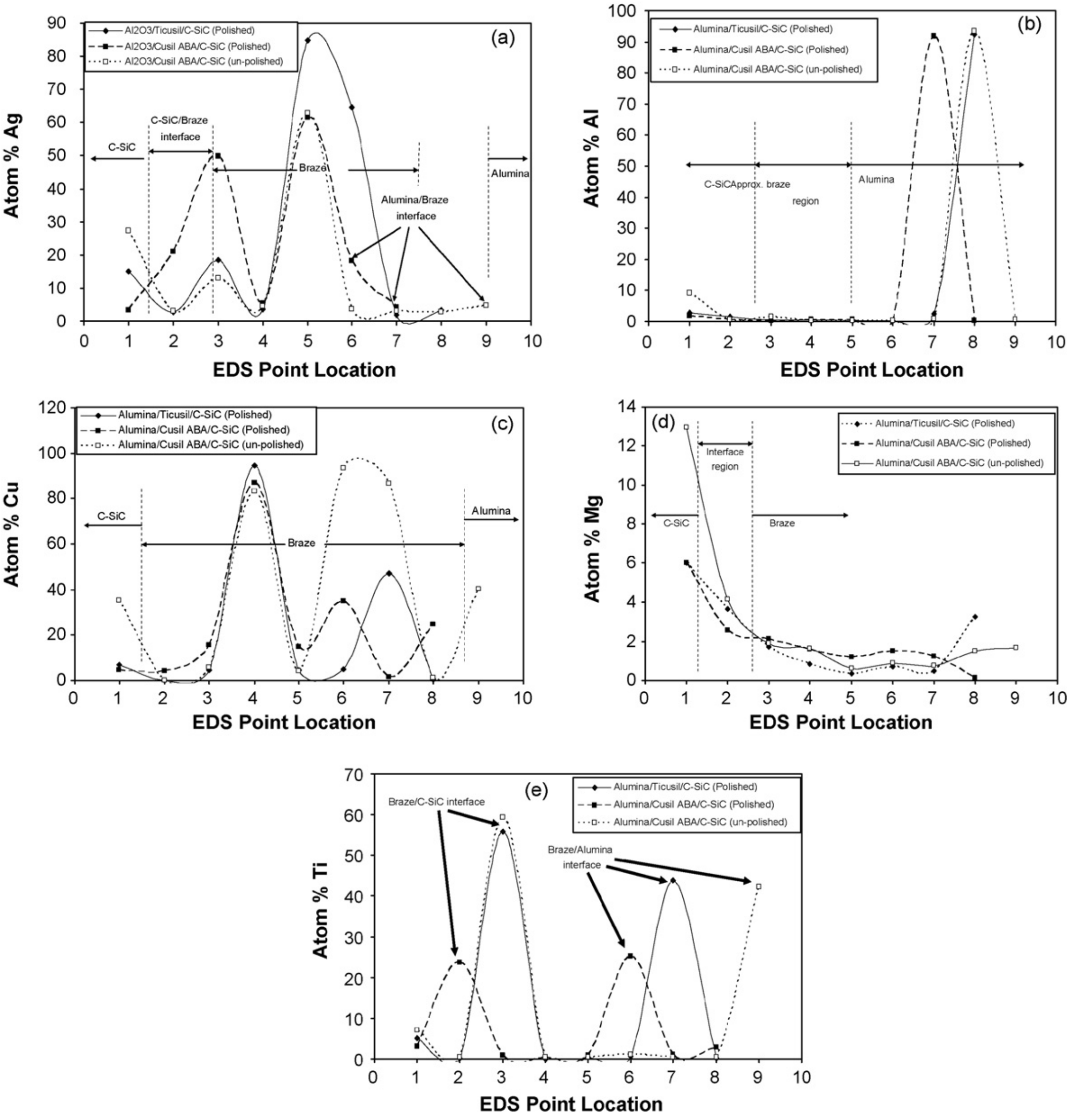

Fig. 7. Relative atomic percentages of major alloying elements in Al_2O_3/C–SiC joints made with Cusil–ABA and Ticusil: (a) Ag, (b) Al, (c) Cu, (d) Mg and (e) Ti. The EDS locations are shown in Fig. 6. The boundaries marked between different regions of the joint are approximate. The curves connecting the data points are not meant to imply a trend.

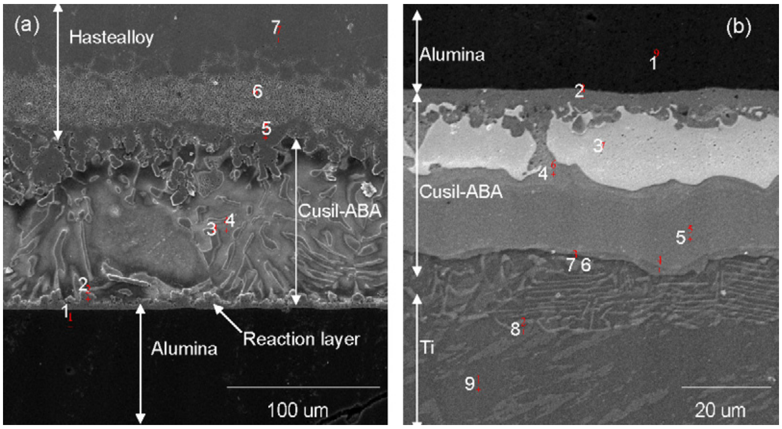

Fig. 8. (a) A Hastealloy/Al_2O_3 joint made using Cusil–ABA and (b) a titanium/Al_2O_3 joint made using Cusil–ABA. The Al_2O_3 substrates were sintered at 1673 K for 2 h.

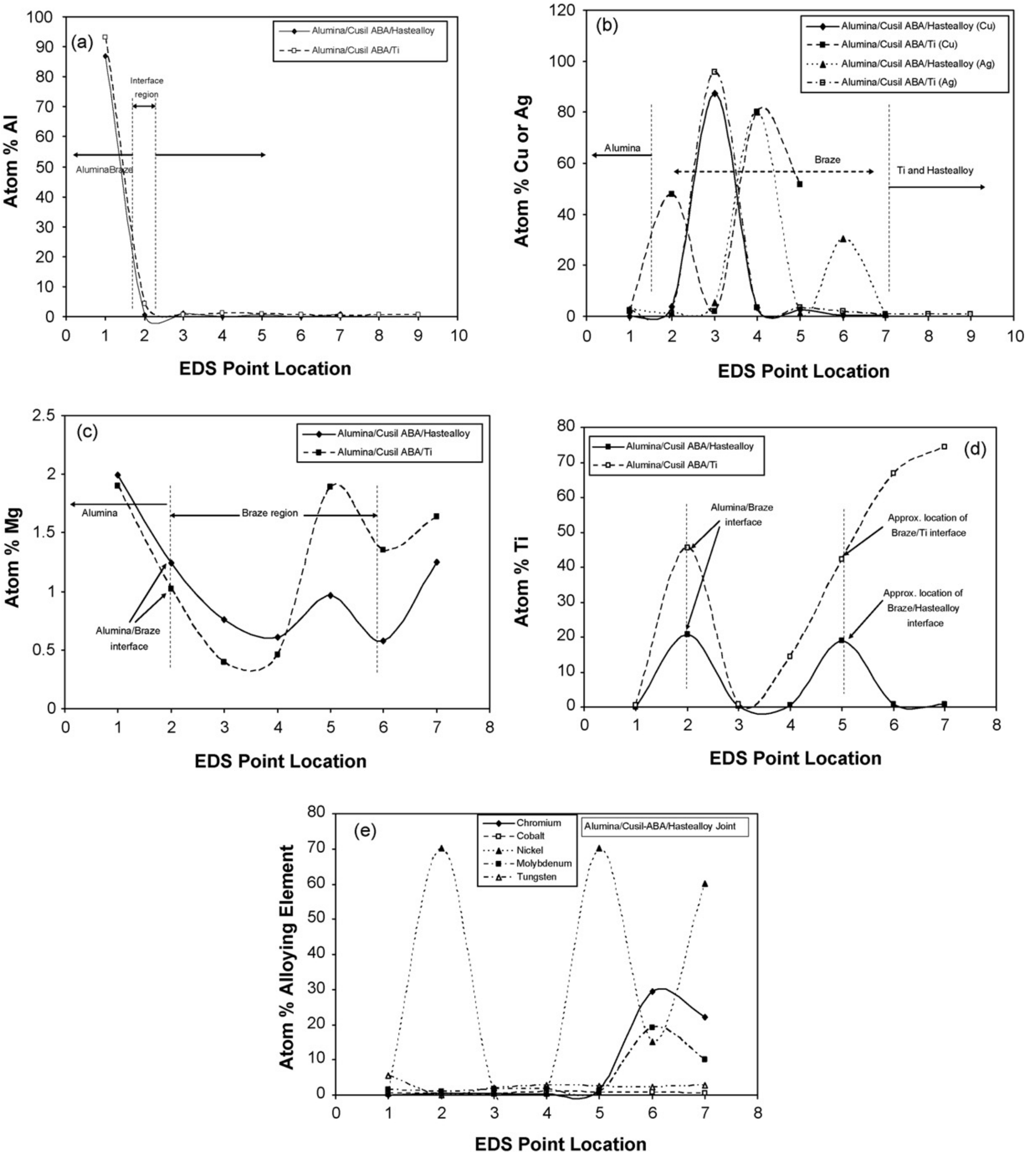

Fig. 9. Relative atomic percentages of major alloying elements across the joint interfaces in alumina/Cusil–ABA/Ti and alumina/Cusil–ABA/Hastealloy joints: (a) Al, (b) Cu and Ag, (c) Mg, (d) Ti and (e) Cr, Co, Ni, Mo and W. The EDS locations are shown in Fig. 8. The boundaries marked between different regions of the joint are approximate. The curves connecting the data points are not meant to imply a trend.

composite joints using Cusil–ABA and Ticusil are shown in Fig. 10(c).

The distribution of microhardness essentially represents a convolution of several factors. A major contributor is the residual thermal stresses caused during brazing by the mismatch of coefficients of thermal expansion (CTE) of the joined materials. The CTE of sintered alumina is ~7.0–7.4 × 10^{-6}/C (90–99.9% pure alumina) and the CTE of Cusil–ABA and Ticusil brazes are significantly larger (18.5 × 10^{-6}/C). A large CTE mismatch may cause a substantial amount of thermal stress to build up in the Al_2O_3/braze/Al_2O_3 joints during brazing. However, it is possible that the presence of reaction-formed oxide compounds TiO and Ti_3Cu_3O at the Al_2O_3/AgCuTi interface may aid thermal stress accommodation[9] because of a gradual transition in CTE from Al_2O_3 (7.0–7.4 × 10^{-6}/C) to TiO (9.2 × 10^{-6}/C) and Ti_3Cu_3O (15.1 × 10^{-6}/C) to Cusil–ABA or Ticusil (18.5 × 10^{-6}/C). A similar gradual transition will be expected for the Al_2O_3/braze/Ti joints. For the Al_2O_3/C–SiC composite joints, the in-plane CTE (α) of CVI C–SiC composites is ~3.63–4.35 × 10^{-6}/C over the temperature range of 20–1250 °C and CTE perpendicular to the plane is 2.18–3.99 × 10^{-6}/C over the range of 20–1250 °C. For the

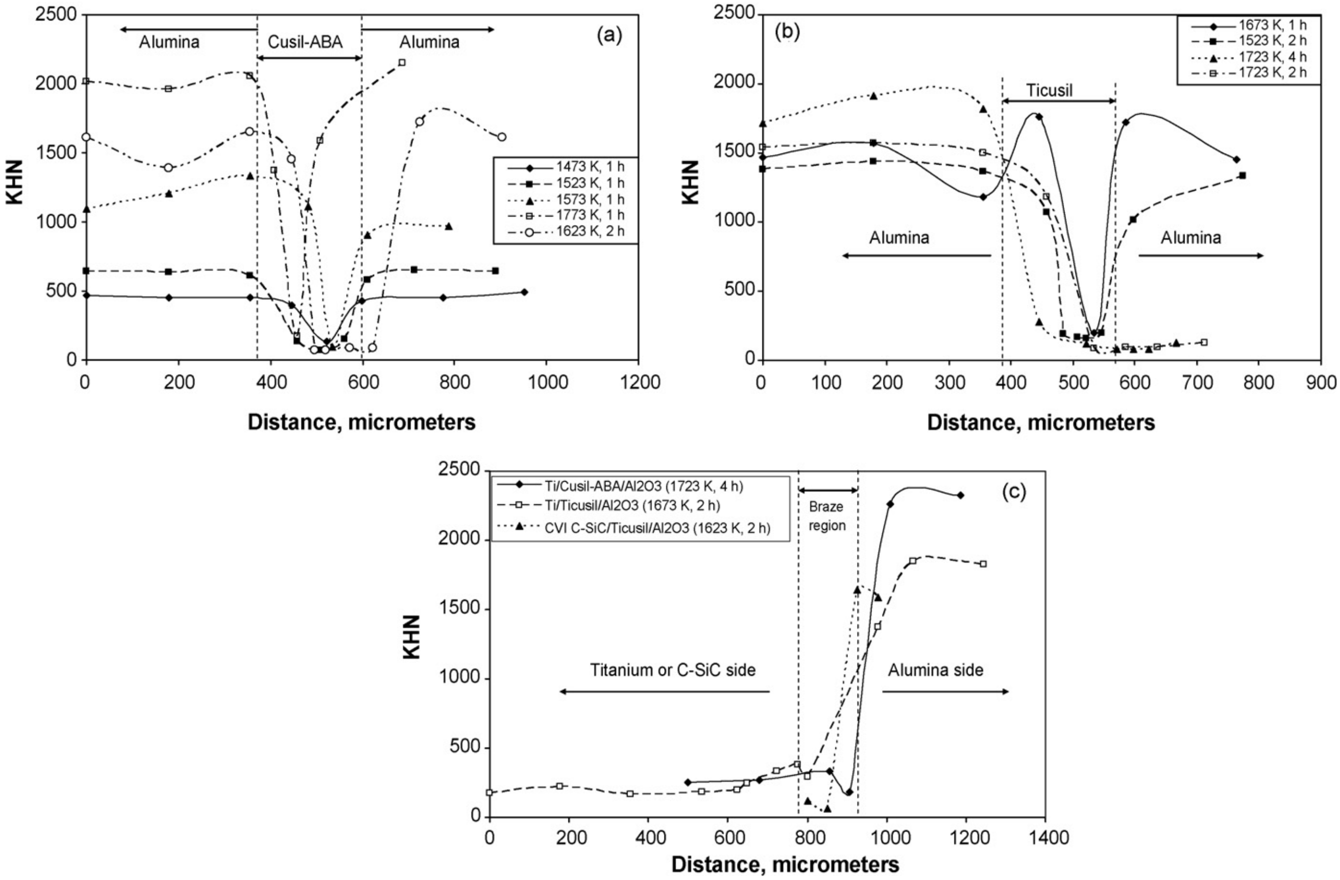

Fig. 10. Distribution of Knoop microhardness across the joint interfaces in various composites: (a) alumina/Cusil–ABA/alumina, (b) alumina/Ticusil/alumina and (c) Ti/Cusil–ABA/alumina, Ti/Ticusil/alumina and C–SiC/Ticusil/alumina joints.

Al_2O_3/Hastealloy joints, the CTE of Hastealloy can be taken approximately to be in the range for Ni-base superalloys (Inconel 625: 12.8×10^{-6}/C, Monel 400: 13.9×10^{-6}/C and Haynes 25: 12.3×10^{-6}/C). These CTE values of the joint materials show that considerable thermal strains will occur in the joined materials. A rough estimate of the thermal strains can be obtained by estimating the product $\Delta\alpha\Delta T$, where $\Delta\alpha$ is the mismatch of CTE (α) between the joined materials and ΔT is the temperature range. Using average values of the CTE of the materials given above, and taking the maximum value of ΔT to be 870° for brazing, the elastic thermal strains are obtained as $\sim 0.28 \times 10^{-2}$ and $\sim 0.54 \times 10^{-2}$ for the Al_2O_3/C–SiC and Al_2O_3/Hastealloy joints, respectively. These large strains may be accommodated by the plastic flow of the relatively ductile Ag–Cu brazes, thus preventing decohesion and joint failure. In addition, any new phases formed at the interface due to chemical reactions with CTE values intermediate between the braze alloy and C–SiC composite (or Hastealloy) will further reduce the thermal stress gradients across the joint.

4. Conclusions

Polycrystalline alumina substrates fabricated using conventional powder metallurgy techniques (powder compaction and sintering) and designed to contain varying levels of porosity via control of sintering conditions were joined to themselves, titanium, Hastealloy X and CVI C–SiC composites using Ti-containing active metal brazes, Cusil–ABA and Ticusil. The alumina substrates with high porosity contents that were achieved by low-temperature sintering treatment exhibited braze infiltration whereas no reactive penetration occurred in dense Al_2O_3 substrates sintered at high temperatures. Chemical reactions and mass transport accompanying molten braze penetration of porous substrates and/or thermally activated diffusion processes led to a Ti-rich reaction product layer at the interface which promoted interfacial bonding. Polishing of CVI C–SiC composites led to better quality Al_2O_3/C–SiC composite joints and greater segregation of Ti at the composite/braze interface than unpolished C–SiC composite specimens. The Knoop microhardness profiles across the joint region displayed a minimum in the braze region and a maximum in the ceramic region, with a relatively sharp discontinuity at the joint interfaces.

Acknowledgements

The authors would like to thank Jennifer Cerny for her help with the microscopy work. R. Asthana acknowledges the research support received from the NASA Glenn Research Center, Cleveland, OH, USA.

References

1. Levi, C. G., Bamberger, M. and Kaplan, W. D., Wetting of porous titanium carbonitride by Al–Mg–Si alloys. *Acta Mater.*, 1999, **47**(14), 3927–3934.
2. Taranets, N. Yu. and Jones, H., Wettability of aluminum nitride-based ceramics of different porosity by two active silver-based brazing alloys. *Mater. Sci. Eng.*, 2004, **A379**, 251–257.
3. Shinozaki, N., Kaku, H. and Mukai, K., Influence of pores on wettability on zirconia ceramics by molten Mn. *Trans. Joining Weld. Res. Ins. Osaka Univ. WRI, Jpn.*, 2001, **30**, 161–166 [special issue].
4. Sobczak, N., Sobczak, J., Rohatgi, P., Ksiazek, M., Radziwill, W. and Morgiel, J., Interactions between Ti or Cr containing Cu alloys and porous graphite substrate. In *Proceedings of the high temperature capillarity conference*, ed. N. Eustathopoulos and N. Sobczak. Foundry Research Institute, Krakow (Poland), 1997, pp. 145–151.
5. Nono, M. C. A., Barroso, J. J. and Castro, P. J., Mechanical behavior and microstructural analysis of alumina–titanium brazed interfaces. *Mater. Sci. Eng. A*, 2006, **435–436**, 602–605.
6. Kingery, W. D., Bowen, H. K. and Uhlmann, D. R., *Introduction to Ceramics* (*2nd ed.*). John Wiley & Sons Inc., New York, 1976.
7. Sobczak, N., Singh, M. and Asthana, R., High-temperature wettability measurements in ceramic-metal systems: some methodological issues. *Curr. Opin. Solid State Mater. Sci.*, 2005, **9**(4–5), 241–253.
8. Asthana, R., Singh, M. and Sobczak, N., Infiltration processing of ceramic-metal composites: the role of wettability, reaction and capillary flow. *J. Kor. Ceram. Soc.*, 2005, **42**(11), 703–717.
9. Mandal, S., Kumar, A. and Ray, A. K., Correlation between the mechanical properties and the microstructural behavior of Al_2O_3–(Ag–Cu–Ti) brazed joints. *Mater. Sci. Eng.*, 2004, **A383**, 235–244.
10. Santella, M. A., Horton, J. A. and Pak, J. J., *J. Am. Ceram. Soc.*, 1990, **73**(6), 1785.
11. Voytovich, R., Ljungberg, L. Y. and Eustathopoulos, N., The role of adsorption and reaction in wetting in the CuAg–Ti/alumina system. *Scripta Mater.*, 2004, **51**, 431–435.
12. Nicholas, M. G. and Peteves, S. D., Reactive joining: chemical effects on the formation and properties of brazed and diffusion bonded interfaces. *Scripta Mater.*, 1994, **31**(8), 1091–1096.
13. Eustathopoulos, N., Drevet, M. and Nicholas, M. G., *Wettability at High Temperatures*. Pergamon, 1998.
14. Asthana, R., Interface- and diffusion-limited capillary rise of a reactive melt with a transient contact angle. *Metall. Mater. Trans.*, 2002, **33A**, 2119–2128.
15. Messner, R. P. and Chiang, Y. M., Liquid-phase reaction bonding of SiC using alloyed Si–Mo melts. *J. Am. Ceram. Soc.*, 1990, **73**(5), 1193–1200.
16. Saiz, E. and Tomsia, A. P., Kinetics of metal-ceramic composite formation by reactive penetration of silicates with molten Al. *J. Am. Ceram. Soc.*, 1988, **81**(9), 2381–2393.
17. Martins, J. P. and Margarido, F., The cracking shrinking model for solid–fluid reactions. *Mater. Chem. Phys.*, 1996, **44**, 156–169.
18. Szekely, J. and Evans, J. W., A structural model for gas–solid reactions with a moving boundary. *Chem. Eng. Sci.*, 1970, **25**, 1091–1097.
19. Sobczak, N., Singh, M. and Asthana, R., editors. High-temperature capillarity and interfacial phenomena. *Curr. Opin. Solid State Mater. Sci.*, August/October 2005, **9**(4–5), 149–151.
20. Asthana, R., On reactive capillary flow with a dynamic contact angle. *J. Mater. Process. Manuf. Sci.*, 2003, **10**(4), 187–197.
21. Asthana, R., Dissolutive capillary penetration with expanding pores and transient contact angles. *J. Colloid Interf. Sci.*, 2000, **231**, 398–400.
22. Asthana, R., Singh, M. and Sobczak, N. The role of wettability and interfacial phenomena in infiltration processing of ceramic-metal composites. In: Zhu, D. and Plucknett, K., editors. *Ceram. Eng. Sci. Proc.*, 2005, **26**(3), 249–261.
23. Sangsuwan, P., Tewari, S. N., Gatica, J. E., Singh, M. and Dickerson, R., Reactive infiltration of silicon melt through microporous amorphous carbon performs. *Metall. Trans.*, 1999, **30B**, 933–944.
24. Martins, G. P., Olson, D. L. and Edwards, G. R., Modeling of infiltration kinetics for liquid metal processing of composites. *Metall. Trans.*, 1988, **19B**, 95–101.
25. Battezatti, L. and Greer, A. L., *Acta Metall. Mater.*, 1989, **37**, 1791.
26. Murr, L. E., *Interfacial Phenomena in Metals and Alloys*. Addison–Wesley, 1975.
27. Singh, M., Asthana, R. and Shpargel, T. P., Brazing of C–C composites to Cu-clad Mo for thermal management applications. *Mater. Sci. Eng. A*, 2007, **452–453**, 699–704.
28. Morscher, G. N., Singh, M., Shpargel, T. P. and Asthana, R., A simple test to determine the effectiveness of different braze compositions for joining Ti tubes to C/C composite plates. *Mater. Sci. Eng. A*, 2006, **18**(1–2), 19–24.
29. Singh, M., Shpargel, T. P., Morscher, G. N. and Asthana, R., Active metal brazing and characterization of brazed joints in titanium to carbon–carbon composites. *Mater. Sci. Eng. A*, 2005, **412**, 123–128.
30. Singh, M., Shpargel, T. P., Morscher, G. N. and Asthana, R., Effect of composite substrate properties on the mechanical behavior of brazed joints in metal-composite system. In *Brazing and soldering, third international conference on brazing and soldering*, ed. J. J. Stephens and K. Scott Weil. ASM International and AWS, 2006, pp. 246–251.
31. Singh, M. and Asthana, R., Joining of ZrB_2-based ultra-high temperature ceramic composites using metallic glass interlayers. *Mater. Sci. Eng. A*, 2007, **460–461**, 153–162.
32. Singh, M., Shpargel, T. P. and Asthana, R., Brazing of stainless steels to yttria-stabilized-zirconia (YSZ) using gold-base brazes for SOFC applications. *Int. J. Appl. Ceram. Tech.*, 2007, **4**(2), 119–133.
33. Asthana, R., Singh, M. and Shpargel, T. P., Brazing of ceramic–matrix composites to titanium using metallic glass interlayers. In: Wereszczak, A., Lara-Curzio, E. and Tandon, R., editors. *Ceramic Eng. Sci. Proc.*, 2006, **27**(2), 159–168.
34. Singh, M., Shpargel, T. and Asthana, R., Brazing of stainless steel to yttria-stabilized-zirconia (YSZ) using silver-base brazes. In: Zhu, D. and Plucknett, K., editors. *Ceramic Eng. Sci. Proc.*, 2005, **26**(3), 383–390.
35. Moorehead, A. J., Elliott Jr., J. H. and Kim, H. E., Brazing of ceramic and ceramic-to-metal joints. *Met. Handbook*, Brazing, ASM International.
36. Sobczak, N. and Asthana, R., The role of wetting phenomenon in the structure and bonding of metal-ceramic interfaces: some recent developments. *Recent Research Developments in Materials Science*, *vol. 2*. Research Signpost, Trivandrum (India), 2001, 135–160.